JOURNAL OF AIRCRAFT
Vol. 31, No. 4, July–Aug. 1994

Side-Force Control on a Diamond Forebody at High Angles of Attack

Dhanvada M. Rao* and Gautam Sharma†
ViGYAN Inc., Hampton, Virginia 23666

A high-alpha side-force control concept for diamond cross section forebodies was investigated. A full-length strake is deployed on one of the lower facets to force a large-scale separation vortex adjacent to the forebody surface, whose suction provides side force across a broad high-alpha range. A simultaneous reduction of the leeside vortex suction decreases the forebody normal force, leading to pitch-up alleviation and drag reduction as additional high-alpha benefits, particularly when the strakes are deployed on both sides. Low-speed wind-tunnel measurements of surface pressures and six-component forces/moments supported by surface and flowfield visualizations on an isolated diamond forebody model verified the control effectiveness to nearly 70-deg angle of attack, and up to 10-deg sideslip angle.

Nomenclature

A_{REF} = reference area, forebody base
A_S = reference area, strake planform
C_D = drag coefficient
C_N = normal force coefficient
C_P = static pressure coefficient
C_Y = side force coefficient, based on A_{REF}
$C_{Y,S}$ = side force coefficient, based on A_S
α = angle of attack
β = angle of sideslip

Introduction

CONSIDERABLE research has been devoted in recent years to the problem of high-alpha yaw control, in recognition of the growing importance of poststall maneuverability and agility requirements of the next generation combat aircraft. Typical of such aircraft configurations are pointed slender forebodies, where crossflow separations at high angles of attack generate intense longitudinal vortices. The well-known tendency of the forebody primary vortex pair to abruptly become nonsymmetrical creates powerful side forces and associated yawing moments, which can overwhelm the reduced rudder power during high-alpha maneuvers, setting the stage for yaw departure and loss of controlled flight. Management and control of the primary forebody vortices for improved departure resistance and poststall controllability is recognized to have considerable potential for future tactical aircraft, as well as for upgrading the high-alpha capability of in-service fighters.

Previous research has identified a variety of forebody vortex control techniques of varying effectiveness.[1-3] The past investigations, however, concentrated on circular or oval cross sections (e.g., F-5, F-16, and F-18). On the smoothly rounded forebody sections, a progressive asymmetry of crossflow separations can be manipulated using mechanical or pneumatic control devices, thereby producing a modulated side force in either direction. Future combat aircraft and missile configurations, however, are likely to employ forebody cross sections composed of flat surfaces and large-angle chines (Fig. 1) for aerodynamic as well as operational reasons. On these diamond-type sections the crossflow separations being anchored to the salient edges will be less amenable to nonsymmetrical manipulation for side-force generation, requiring a basically different approach than that found successful on the rounded sections.

This article deals with an experimental investigation of a novel vortex-controlled side-force concept proposed for diamond forebodies at high angles of attack. Low-speed wind-tunnel measurements of surface pressures and six-component forces/moments were performed on an isolated forebody model, and supplementary flow visualizations conducted in order to characterize the relatively unexplored high-alpha aerodynamics of diamond-shaped forebodies and for a preliminary quantification of the proposed control concept.

Concept Description

The flow past a diamond cross section forebody at high angles of attack (to anticipate the experimental results presented in the next section) is characterized by attached flow on the lower (windward) facets, separation at the side edges or chines, and vortex roll-up over the upper facets. The geometrically fixed crossflow separations in this case, as already noted, preclude the feasibility of asymmetric manipulation for side-force generation. An alternative approach proposed here was to force a large-scale, three-dimensional separation on one of the lower facets of the forebody, by deploying a longitudinally hinged strake from its conformally stored position (Fig. 2). The resulting vortex is "captured" in the upper corner formed between the strake and the lower facet; its suction on the adjacent surfaces providing the side force. In the assumed flow model (verified experimentally as described in the next section), strake deployment on one side does not

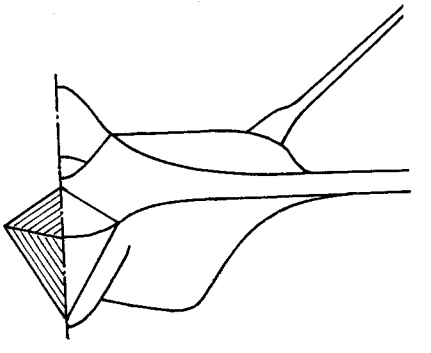

Fig. 1 Diamond forebody on a contemporary fighter configuration.

Received June 14, 1993; presented as Paper 93-3407 at the AIAA 11th Applied Aerodynamics Conference, Monterey, CA, Aug. 9–11, 1993; revision received Oct. 29, 1993; accepted for publication Oct. 30, 1993.

*Principal Vice President. Associate Fellow AIAA.
†Research Engineer. Member AIAA.

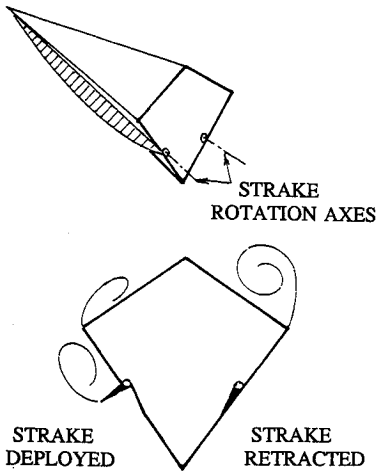

Fig. 2 Diamond forebody side-force control concept.

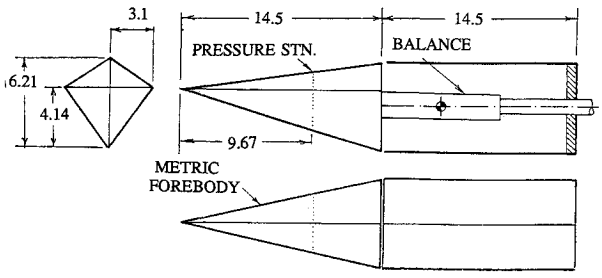

Fig. 3 Diamond forebody wind-tunnel model geometry (dimensions in inches).

affect the prevailing attached flow on the opposite lower facet, resulting in a substantial circumferential pressure asymmetry, therefore generating a side force towards the deployed strake. At the same time, the vortex suction on the lower facet, supplemented by reduction of leeside suction creates a downward normal-force component, creating a potential for pitch-up alleviation. Symmetrical deployment of both strakes tends to reinforce the normal-force reduction, thus providing powerful pitch-down control with a net zero side force. This dual yaw/pitch capability is unique to the present strake concept, in contrast to the previous forebody devices limited to yaw control.

Experimental Details

The diamond forebody geometry adopted for the present investigation is shown in Fig. 3. This generic configuration consisted of a conical nose section followed by a parallel afterbody. The conical part with geometrically similar cross sections and straight-line generators was mounted at the front end of a six-component strain-gauge balance. A nonmetric, constant-section afterbody functioned as a balance shield, and also served to isolate the metric forebody flowfield from blunt-base separation effects. A transverse row of static-pressure orifices was installed on all four facets in a common cross section plane, and connected to an external Scani-Valve system.

A series of forebody strake shapes tested is shown in Fig. 4. The flat-plate strakes were attached to the conical forebody along a ray bisecting the lower facet, and simulated a 90-deg deployment angle relative to the facet. Some of the strakes were tested in nonsymmetrical (left and right), as well as symmetrical (both side) arrangements.

Pressure, balance, and oil flow tests were performed in the ViGYAN 3- by 4-ft low-speed wind tunnel at a freestream velocity of 65 ft/s, corresponding to a Reynolds number of 0.5×10^6 based on the metric forebody length (or 0.25×10^6 based on its maximum width). From the known Reynolds number independence of the two-dimensional drag of diamond-section cylinders (see Fig. 5 taken from Ref. 4), the diamond forebody crossflow characteristics are anticipated to be relatively free from scale effect, in contrast to the circular cylinder with its well-known critical transitional behavior.

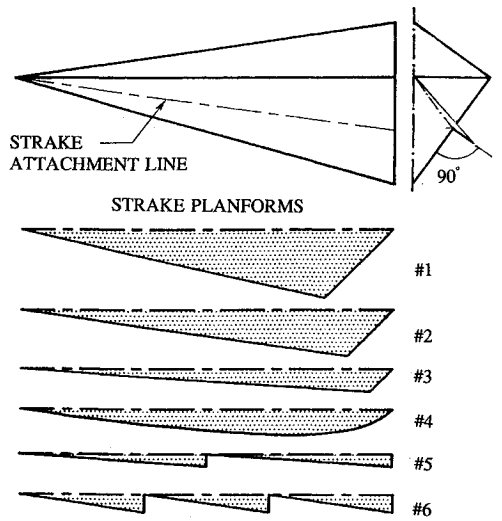

Fig. 4 Forebody strake attachment and planforms.

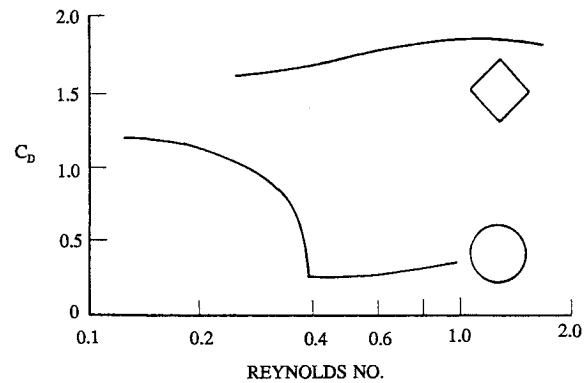

Fig. 5 Two-dimensional drag coefficient vs Reynolds number of circular and diamond cross section cylinders (from Ref. 4).

The smoke visualizations were conducted on the same model in the ViGYAN 1.5- by 1.5-ft smoke tunnel at an estimated speed of 1 ft/s. Smoke was released through a row of small-diameter ports in the forebody (located just below the strake attachment line) to be drawn into the strake vortex; the vortex cross section was visualized in a transverse light sheet positioned in the pressure measurement cross-plane. Video records and still photographs were taken in a range of alpha.

Results and Discussion

Surface Pressures and Flow Visualizations

Selected pressure results and flow visualizations are presented for a preliminary validation of the side-force control concept, which also serve as a backdrop to the balance data discussed in the following section. Circumferential pressure distributions on the baseline model (i.e., forebody without strakes) at increasing angles of attack are presented in Fig. 6. The positive pressures on the two lower facets are associated with attached flow, which evidently persists throughout the alpha range. On the upper facets, negative pressures are generated by side-edge separations, the suction peaks indicating the presence of a vortex pair. Flow attachment due to the downwash between the leeward vortices reduces the suction level over the middle region. Unequal growth of the leeside suction peaks with increasing angle of attack indicates the development of vortex asymmetry up to at $\alpha = 60$ deg, above which the uniformity of suction across the upper surfaces suggests the onset of a two-dimensional, wake-like flow.

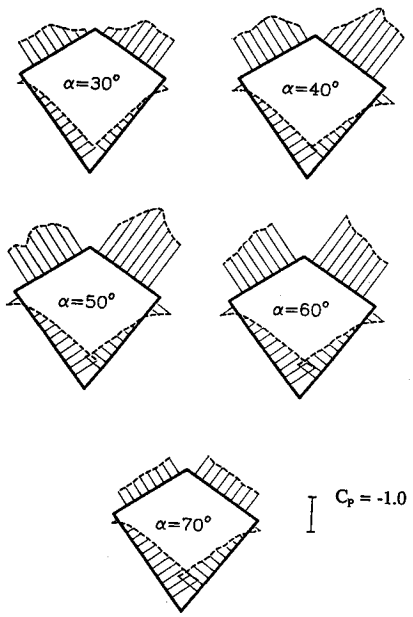

Fig. 6 Baseline forebody circumferential pressure distributions at increasing angle of attack.

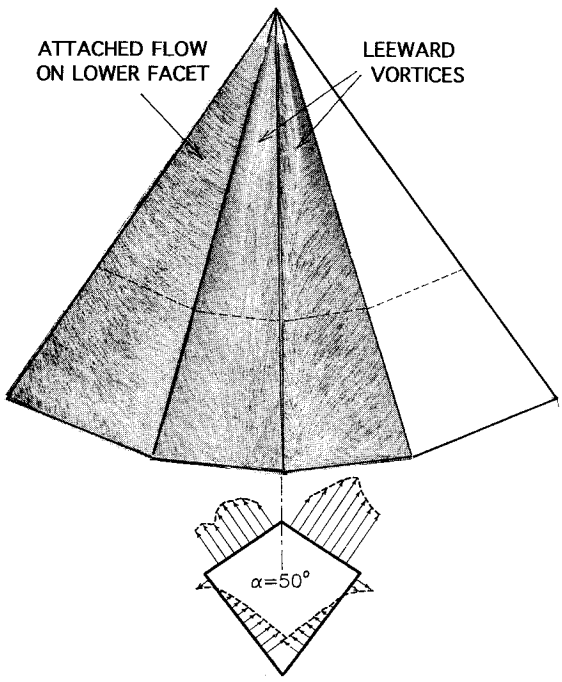

Fig. 7 Baseline forebody oil flow visualization and circumferential pressure distribution at α = 50 deg.

A typical oil-flow visualization at α = 50 deg, and corresponding pressure distribution shown in Fig. 7, support the above description of the diamond forebody high-alpha flow characteristics.

Next, the effect of a left-strake deployment on the circumferential pressure distribution is illustrated in Fig. 8. Noteworthy effects of strake deployment are the onset of pronounced suctions above the strake-attachment line and increased positive pressures below it, while the lower-facet pressures on the opposite side of the forebody remain unchanged. The resulting lateral asymmetry in the circumferential surface pressures of the forebody and the pressure-differential on the strake itself (as indicated by the pressure jump across the strake root) will combine to produce a left-directed side force. These sectional pressure results presage a substantial high-alpha side-force capability of the strake concept, continuing to α = 60 deg.

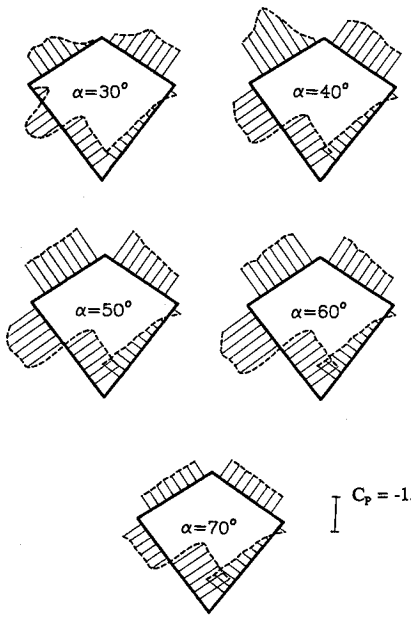

Fig. 8 Circumferential pressure distributions with a typical left strake deployment at increasing angle of attack.

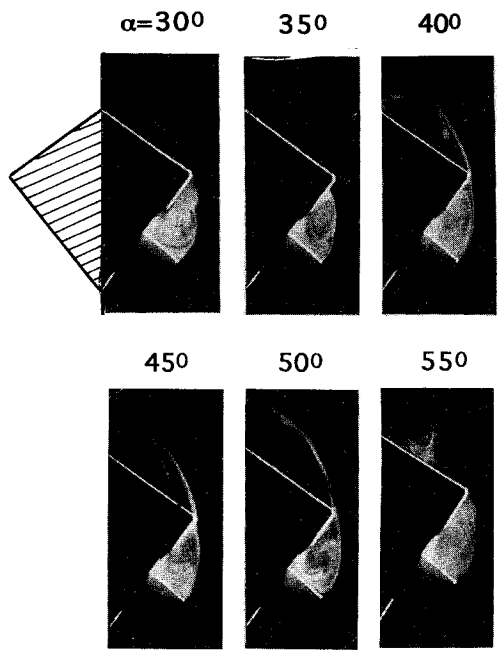

Fig. 9 Crossflow plane visualizations with typical right strake deployment at increasing angle of attack.

A sequence of cross-plane smoke visualizations with right-deployed strake at increasing angles of attack is presented in Fig. 9. Clearly defined is a large-scale vortex filling the upper strake/forebody corner, in accordance with the postulated flow model, through angles of attack to 50 deg. At higher alphas, the expanding vortex cross section culminated in the shedding of the core to the upper facet. Even after the strake vortex migration to the leeside, a steady three-dimensional separation bubble continued to span the strake and forebody side corner, whose suction effect is anticipated to allow side force to persist almost to 70-deg alpha.

An oil-flow visualization with a left-deployed strake (no. 3) obtained at 50-deg angle of attack is shown in Fig. 10. The lower-surface pattern clearly reveals the vortex footprint occupying the full width between strake attachment line and the corresponding side corner. Simultaneously, the strake-side lee vortex shrinks considerably in comparison with the opposite lee vortex. Additional oil-flow visualizations presented in Fig.

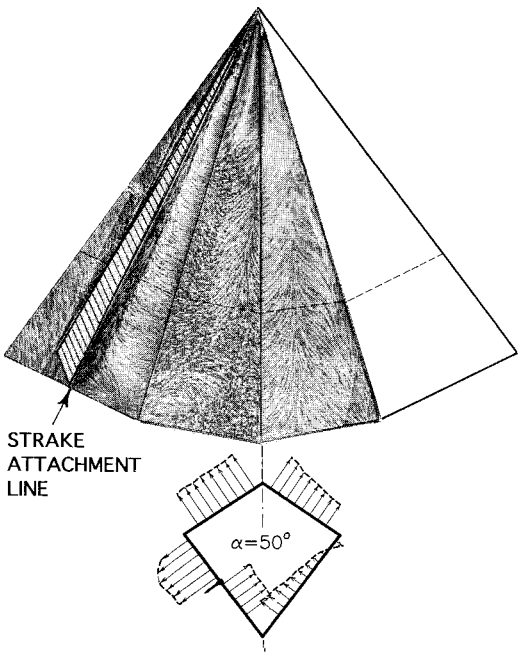

Fig. 10 Oil flow visualization and circumferential pressure distribution with a typical left strake deployment at α = 50 deg.

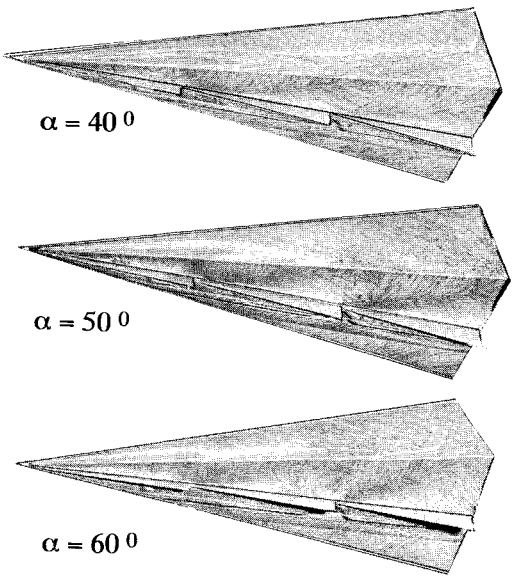

Fig. 11 Oil flow visualizations with left deployed saw tooth strake no. 6 at increasing angles of attack.

11 show vortices in tandem generated by the sawtooth strake no. 6 at angles of attack 40, 50, and 60 deg. These observations suggest that unconventional strake planforms might be used to more effectively capture the vortex suction over most of the forebody length throughout the high-alpha range, while allowing the strake size (surface area) to be reduced significantly.

Finally, a sequence of circumferential pressure distributions with both strakes symmetrically deployed at increasing alpha is presented in Fig. 12. As expected, the pressure distributions remain laterally symmetrical with pronounced suction peaks appearing on both the windward facets. Of particular interest is the reduction of average upper-surface suction levels in comparison with baseline up to α = 60 deg (Fig. 13), which corroborates flow visualization results of leeside vortex reduction consequent to strake deployment. The combined effect of reduced leeward suction and the lower-surface strake vortex suction can be anticipated to produce a significant normal-force relief on the forebody.

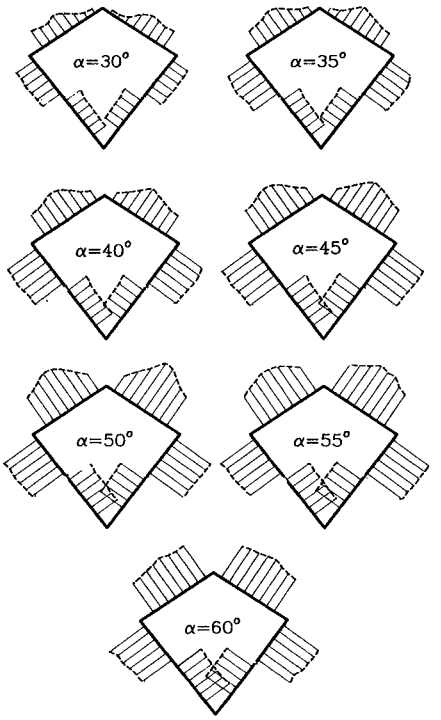

Fig. 12 Circumferential pressure distributions with symmetrically deployed strakes no. 4 at increasing angle of attack.

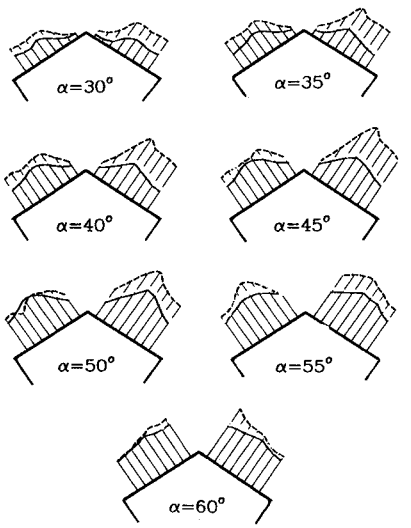

Fig. 13 Upper surface pressure distributions with symmetrically deployed strakes no. 4 at increasing angle of attack, compared with baseline.

Balance Measurements

Side-force characteristics with increasing alpha of various left-deployed strakes are presented in Fig. 14. In all cases, the side-force capability is seen to start as early as α = 10 deg, and reach a maximum around α = 45 deg, followed by a relatively slow decline at the higher angles of attack. With any particular strake the side force is sustained at 70–80% of the maximum value, up to an alpha as high as 60 deg. An associated normal-force reduction is also found (Fig. 15), commencing at about α = 40 deg, and rising to a maximum around α = 55 deg. The maximum side force is found to generally increase in proportion to strake area as indicated in Fig. 16, implying that it is mainly contributed by the strake loading itself. Strake nos. 1 and 2, however, fall well below the area-trend, indicating that they are oversized, i.e., their excessive span forces the vortex out of the lower-surface corner over to the leeside at relatively low angles of attack. The normal-force reduction, also shown in Fig. 16, appears to

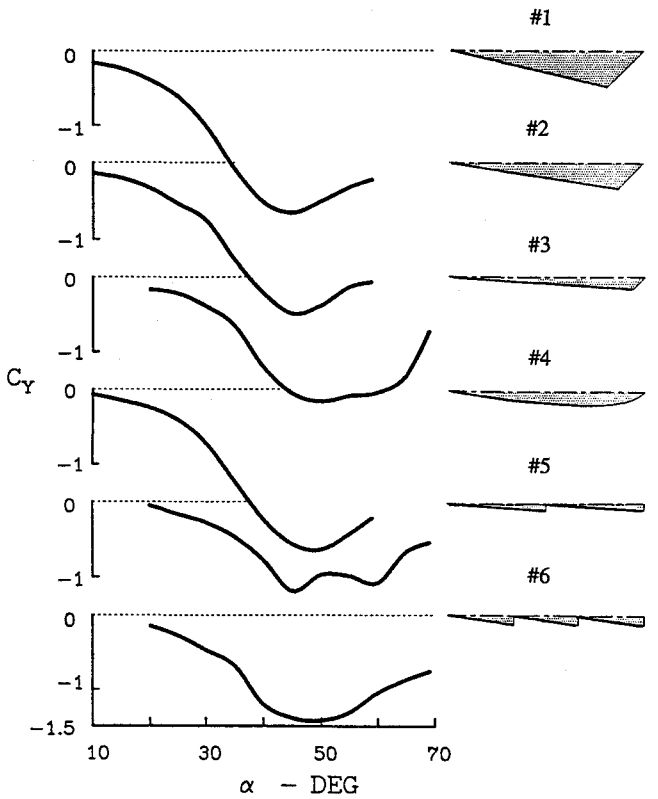

Fig. 14 Side force vs alpha with various left deployed strakes.

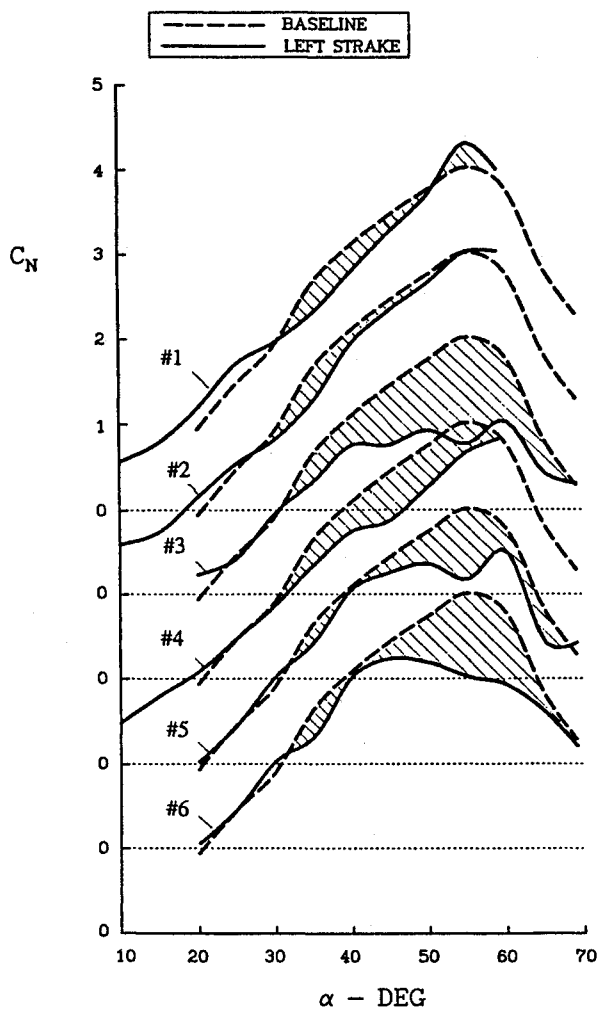

Fig. 15 Normal force vs alpha with various left deployed strakes.

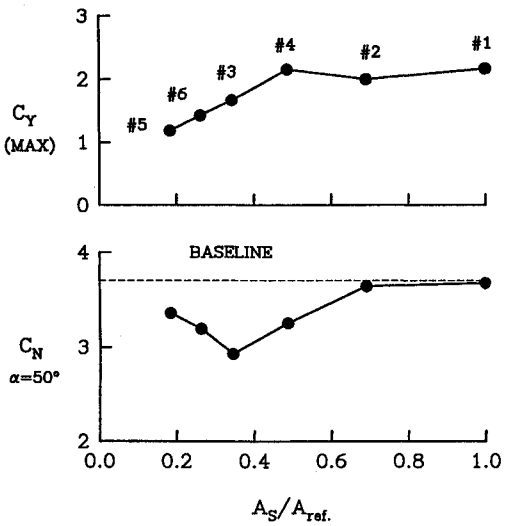

Fig. 16 Maximum side force, and normal force at α = 50 deg, as a function of strake area.

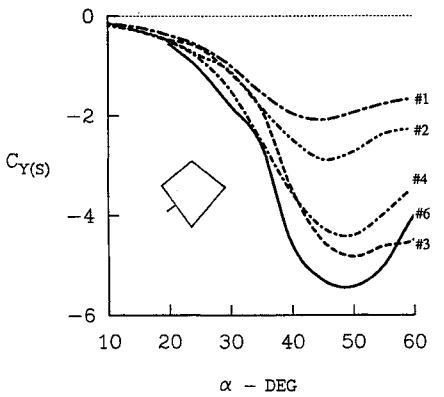

Fig. 17 Side force vs alpha of various left-deployed strakes, referenced to strake area.

follow a contrary trend however, e.g., strake no. 3 produces a substantial reduction, whereas the largest-area strake no. 1 is relatively ineffective. These opposite trends of side force and normal force vs strake area characteristics might be anticipated because, whereas side force arises from a combination of body-suction and strake-load components, the normal force is a net result of the same two components acting in opposition.

A relative measure of the side-force effectiveness of the various strakes of different area is provided by using for reference the individual strake area [A_S rather than a common forebody base area (A_{REF})]. On the A_S basis (Fig. 17) the saw-tooth (no. 6) stands out as the most area-efficient strake, supporting the idea of creating tandem vortices for more effective exploitation of present strake concept. Thus, a saw-tooth strake of optimum surface area (e.g., A_S/A_{REF} = 0.5, see Fig. 16) might combine the benefits of planform shape and area to yield a more efficient strake design. It may be noted that A_S/A_{REF} = 0.5 on a typical aircraft configuration would correspond to a strake of about 1.5% of wing area, which can be regarded to be a practical size for an actuated control surface.

It is of interest to compare the present diamond forebody results with those reported in the literature on circular cross section forebodies. The data of Ref. 3 (which investigated leeside nose-tip strakes for side-force generation), are useful for this purpose because they include independent metric-forebody force measurements. The two forebodies to be compared, however, are of different fineness ratio, a parameter additionally influencing their side-force characteristics. To circumvent the fineness-ratio effect, the ratio C_Y/C_N (which

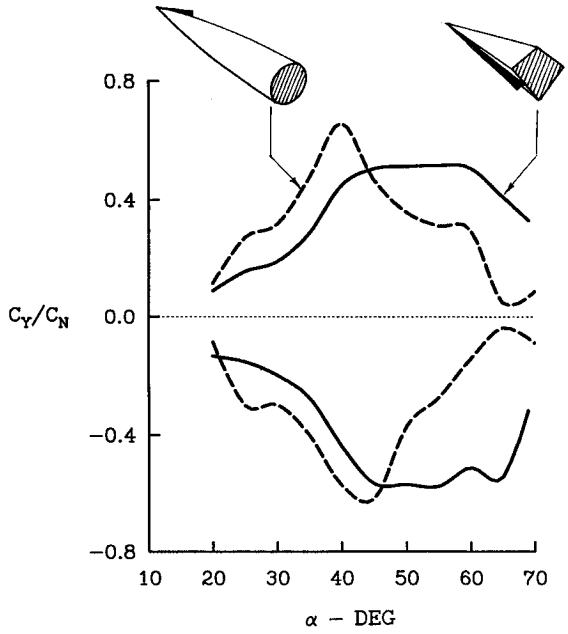

Fig. 18 Comparison of C_Y/C_N vs alpha of circular cross section and diamond forebodies with side-force control.

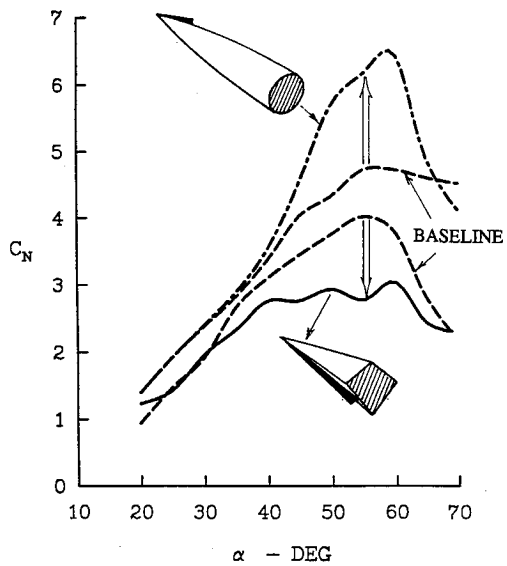

Fig. 19 Comparison of normal force vs alpha of circular cross section and diamond forebodies with side-force control.

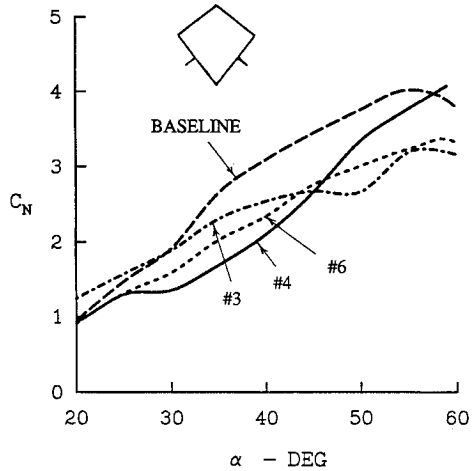

Fig. 20 Normal force vs alpha with symmetrically deployed strakes.

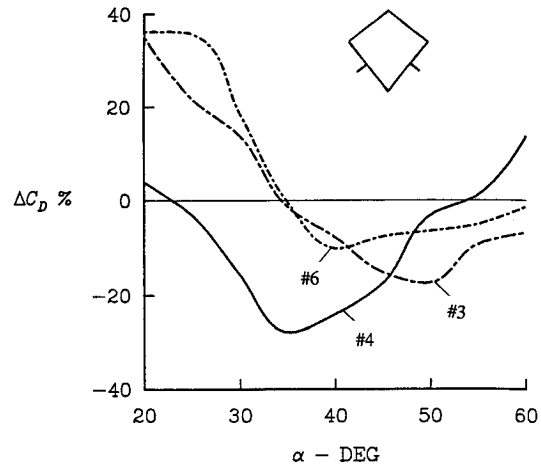

Fig. 21 Diamond forebody drag reduction with symmetrically deployed strakes.

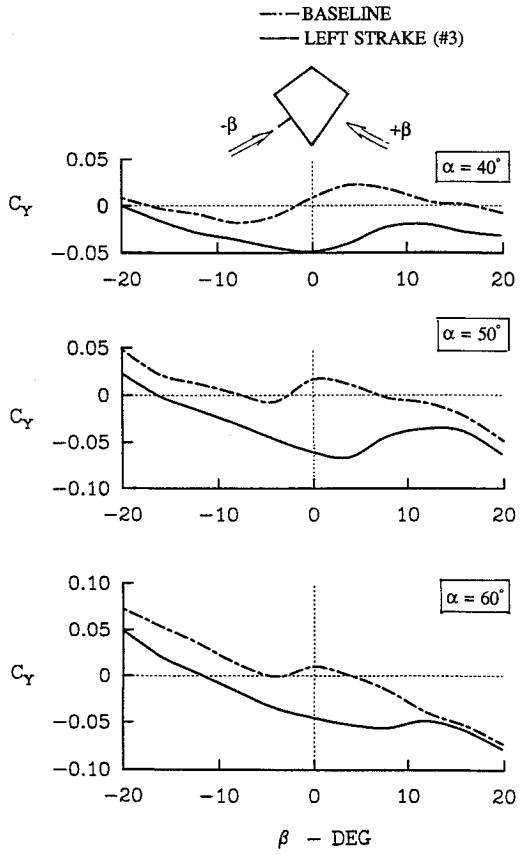

Fig. 22 Side force vs sideslip angle with left deployed strake no. 3.

measures the lateral rotation of the cross-force vector due to forebody flow asymmetry), has been used in place of C_Y in the present comparison. As shown in Fig. 18, although the diamond forebody side-force control initially develops comparatively slowly with increasing alpha, at $\alpha > 45$ deg and to nearly 70 deg (i.e., well into the post-stall regime), its side-force capability is better sustained than by nose-tip strakes on the circular forebody. A normal force comparison of the two forebodies with their respective side-force control devices (Fig. 19) reiterates the unique advantage of the present concept, viz., a normal-force reduction accompanying the side force in contrast to the ogive forebody where the normal force increase with nose-strake deployment.

Symmetrical strake deployment, i.e., at equal angle on both sides of the diamond forebody, can be expected to generate a pure pitch-down moment due to normal-force reduction, as already foreshadowed in the circumferential pressure distri-

butions of Fig. 12. The normal force characteristics vs alpha of three different strake designs in symmetrical arrangement are shown in Fig. 20. A substantial decrease of the normal force is evident in all three cases, a saw-tooth shape once again emerging as the most effective strake across the alpha range. Corresponding side-force measurements (not presented) confirmed the side force to remain essentially at zero with the symmetrical strakes. The reduced normal force at constant alpha directly yields a drag reduction on the forebody, to the extent of 20–30% in this instance (Fig. 21). In applications (e.g., cruise missiles) where a diamond-section forebody may contribute a significantly higher proportion to the total drag during high-alpha maneuvers (see Fig. 5), this magnitude of drag reduction may be of substantial benefit.

Any practical side-force control device must remain effective during the large sideslip excursions inherent to hard maneuvering. The side-force capability of the left-deployed strake no. 3 in the sideslip range $\alpha = -20$ to $+20$ deg, and at three angles of attack, is shown in Fig. 22. Although the strake-generated side force declines with increasing beta, at least 50% of the zero-beta control is retained at $\beta = +5/-5$ deg. With the strake deployed on the same side as sideslip (i.e., the windward side), however, significant side-force control is maintained up to β approaching 20 deg.

Concluding Remarks

An exploratory low-speed wind-tunnel investigation was conducted of a high-alpha side-force control concept for application to forebodies of diamond cross section. A root-hinged strake is deployed along one of the forebody lower facets to create a large-scale separation vortex, whose suction provides sustained side force to nearly 70-deg angle of attack. Simultaneously, the lee-surface suctions are lowered which, in concert with the strake-induced suction on the windward surface, reduces the forebody normal force. Symmetrical deployment of both the strakes augments normal-force reduction with zero net side force, offering the prospects of pitch-up and drag alleviation on the forebody at high (i.e., post-stall) angles of attack. These salient features of the side-force control concept were verified in low-speed tunnel tests on an isolated diamond forebody model via surface pressure and six-component balance measurements and flow visualizations. A series of strake designs evaluated for area and planform effects indicated potential for further improvements in control effectiveness through strake geometry optimization. Other parameters of equal importance, viz., strake hinge-line placement on the lower facet, strake length, deployment angle, etc., not included in this preliminary study, require investigation to complete the optimization process. The successful feasibility demonstration on an isolated forebody model of this study warrants a more comprehensive evaluation of the side-force concept on a complete aircraft or missile configuration including investigation of tail-buffet as well as Reynolds and Mach number effects.

Acknowledgments

This research was supported by Flight Dynamics Directorate, Wright Laboratory, Wright-Patterson AFB, OH, under a Small Business Innovative Research (Phase I) Program, with Larry W. Rogers as the Technical Monitor.

References

[1]"High-Angle-of-Attack Projects and Technology Conf.," NASA CP 3137, Vol. 3, April 1992.

[2]Rao, D. M., Moskovitz, C., and Murri, D. G., "Forebody Vortex Management for Yaw Control at High Angles of Attack," International Council of Aeronautical Sciences, ICAS-86-2.5.2, Sept. 1986.

[3]Malcolm, G. N., "Forebody Vortex Control," *Progress in Aerospace Sciences*, Vol. 28, Pergamon, 1991, pp. 171–234.

[4]Polhamus, E. C., "Effect of Flow Incidence and Reynolds Number on Low-Speed Aerodynamic Characteristics of Several Noncircular Cylinders with Applications to Directional Stability and Spinning," NASA TR R-29, 1959.